Chapter 8

Luminescent Devices Based on Silicon-Rich Dielectric Materials

Santiago A. Cabañas-Tay, Liliana Palacios-Huerta,
Mariano Aceves-Mijares, Antonio Coyopol,
Sergio A. Pérez-García, Liliana Licea-Jiménez,
Carlos Domínguez and Alfredo Morales-Sánchez

Additional information is available at the end of the chapter

http://dx.doi.org/10.5772/64894

Abstract

Luminescent silicon-rich dielectric materials have been under intensive research due to their potential applications in optoelectronic devices. Silicon-rich nitride (SRN) and silicon-rich oxide (SRO) films have been mostly studied because of their high luminescence and compatibility with the silicon-based technology. In this chapter, the luminescent characteristics of SRN and SRO films deposited by low-pressure chemical vapor deposition are reviewed and discussed. SRN and SRO films, which exhibit the strongest photoluminescence (PL), were chosen to analyze their electrical and electroluminescent (EL) properties, including SRN/SRO bilayers. Light emitting capacitors (LECs) were fabricated with the SRN, SRO, and SRN/SRO films as the dielectric layer. SRN-LECs emit broad EL spectra where the maximum emission peak blueshifts when the polarity is changed. On the other hand, SRO-LECs with low silicon content (~39 at.%) exhibit a resistive switching (RS) behavior from a high conduction state to a low conduction state, which produce a long spectrum blueshift (~227 nm) between the EL and PL emission. When the silicon content increases, red emission is observed at both EL and PL spectra. The RS behavior is also observed in all SRN/SRO-LECs enhancing an intense ultraviolet EL. The carrier transport in all LECs is analyzed to understand their EL mechanism.

Keywords: silicon-rich dielectrics, photoluminescence, electroluminescence, conduction mechanisms

1. Introduction

The use of photonic signals instead of electrons to transmit information through an electronic circuit is an actual challenge. Unfortunately, it is well known that bulk silicon (Si) is an indirect bandgap semiconductor, making it an inefficient light emitter. Therefore, great efforts have been taken to obtain highly luminescent Si-based materials in order to get Si-based photonic devices, especially a light emitting device [1–3]. Such circumstances have led to explore new options for converting silicon into a luminescent material. Si nanoparticles (Si-nps) embedded in a dielectric material as silicon-rich oxide (SRO) or silicon-rich nitride (SRN) show a prominent photoluminescence (PL) emission in red and blue-green region, respectively [4–10]. Thus, SRN or SRO films have been considered as promising candidates for emissive materials due to their potential applications in Si-based optoelectronic devices, and their fully compatibility with the complementary metal-oxide-semiconductor (CMOS) processes [11–16].

Two main strategies have been explored: those that focus on the intrinsic emission from the matrix, either through emissions from defects or by the presence of Si-nps. The second one focus on extrinsic emission, which is produced by doping the material (usually introducing rare earth ions) [3, 17].

The most common strategy to obtain intrinsic emission is through silicon nanostructures, which significantly increase the emission due to the quantum confinement effect (QCE) [5, 18]. Furthermore, the dependence on the size of the Si-nps on the forbidden gap width allows that the emission can be adjusted in the visible and the red-near infrared region of the electromagnetic spectrum [19]. Several studies have reported both red and near infrared electroluminescence (EL) SRO which is mainly attributed to the recombination of excitons in Si-nps [20, 21]. On the other hand, the emission of green or blue light has been attributed to defects associated with oxygen [22, 23]. Some studies have reported that red (620 nm) EL emission could be attributed to non-bridging oxygen hole center (NBOHC) defects whose origin has been corroborated by the fact that the peak position does not change if the film is excited with different energies [24].

Another alternative to obtain intrinsic light emission is through an ordered structure of Si-nps by a superlattice, which is formed by the alternating of SRO and SiO_2 nano-films. Red or near infrared emission has been observed in these structures and has been related to both excitonic recombination taking place in confined states within Si-nps or relaxation of hot electrons [25, 26].

Intrinsic emission has been also observed in SRN films [27–31]. For example, an orange emission at 600 nm was observed at room temperature and has been related to the electron-hole pairs' recombination within Si-nps [27]. Also, green emission has been observed in nitrogen-rich silicon nitride, which was attributed to radiative recombination in localized states related to Si-O [28]. Some other authors have shown significant improvement of the green emission intensity using oxidized silicon-rich nitride [29]. Also, when a silicon nitride film is implanted with Si ions, violet and green-yellow emission bands are observed, giving rise to an intense

white EL emission [30]. The violet band was related with the presence of defects states related to silicon dangling bonds (=Si^0 or centers K^0) located near the middle of the forbidden gap of silicon nitride and defect states related to the unit Si–Si= located near the edge of the valence band, while the green-yellow band was attributed to the transition from the =Si^0 state to nitrogen dangling bonds (=N–) in the tails of valence bands.

Red-near infrared EL (800 nm) has been reported in superlattices combining SRN and SiO_2 films and explained by the bipolar recombination of electron-hole pairs in Si-nps present within the SRN films [31]. A yellow EL emission has been reported when an SRO film instead of SiO_2 layer is used in the multilayer structure [32]. All of these promising results have proved the first implemented all-silicon-based photonic device [33]. Nevertheless, despite all these promising results in luminescent silicon-based materials, the improvement of the efficiency of the light emitting devices is still necessary.

This chapter shows a review about our experience on the PL and EL properties of SRN and SRO films deposited by low-pressure chemical vapor deposition (LPCVD). The effect of the combination of the SRN and SRO luminescent properties is also analyzed as an SRN/SRO structure. A study about the composition, structural, optical, and electro-optical properties of these films will be discussed. The study also includes the analysis of the charge transport mechanism through the SRO, SRN, and SRN/SRO films to understand their electroluminescence behavior and its correlation with the different luminescent centers (LCs) within the active material.

2. Experimental procedure

In this chapter, SRN, SRO, and SRN/SRO films were deposited in a homemade LPCVD hot-wall reactor. In these silicon-rich dielectrics materials, the Si content was controlled by a ratio of partial pressure of reactant gases; R_N and *R*o for SRN and SRO, respectively.

The SRN films were deposited on N-type ((100)-oriented) Si wafers with a resistivity of 1–5 Ω-cm at 750°C using ammonia (NH_3) and 5% nitrogen (N_2)-diluted silane (SiH_4) as the reactant gases by the ratio $R_N = 20*P(NH_3)/P(SiH_4)$. SRN films with R_N values of 5, 20, and 80 were deposited with the parameters shown in **Table 1**. SRO films were deposited on N-type Si wafers with a resistivity of 5–10 Ω-cm ((100)-oriented) at a temperature of 720°C using pure nitrous oxide (N_2O) and 3.3% nitrogen (N_2)-diluted silane (SiH_4) as the reactant gases by the ratio $Ro = 30*P(N_2O)/P(SiH_4)$. SRO films with *R*o values of 30 and 20 were deposited with the parameters shown in **Table 1**. Finally, SRN/SRO bilayers were deposited on P-type silicon substrates ((100)-oriented) with resistivity of 5–10 Ω-cm. *R*o = 20 and 30 and $R_N = 80$ values were used for the SRO and SRN films, respectively. SRO and SRN films were deposited at 730 and 760°C, respectively. The deposition conditions are also summarized in **Table 1**. About 3.3% of nitrogen diluted silane was used for the bilayer structures.

After deposition, SRN, SRO and SRN/SRO samples were thermally annealed at 1100°C under nitrogen atmosphere conditions for 180 min.

	Sample name	R_N	Ro	Pressure of gases (Torr)			Time (min)	Thickness (nm)
				N_2O	NH_3	SiH_4		
SRO	M20		20	0.53		0.80	12	55.72 ± 5.0
	M30		30	0.80		0.80	15	64.00 ± 3.4
SRN	N5	5			0.22	0.85	10	102.83 ± 3.62
	N20	20			0.85	0.85	15	112.67 ± 6.19
	N80	80			2.00	0.50	13	66.93 ± 2.12
SRN/SRO	B20	80			1.08	0.41	4	16.32 ± 1.54
			20	0.53		0.80	15	55.72 ± 5.0
	B30	80			1.08	0.41	4	16.32 ± 1.54
			30	0.80		0.80	15	64.00 ± 3.4

Table 1. Process parameters of the SRO, SRN and SRN/SRO films deposited by LPCVD and thickness of the sample after thermal annealing.

For electrical and electroluminescence studies, light emitting capacitive (LEC) structures were fabricated. For SRN-LECs, a transparent 300-nm thick fluorine-doped tin oxide SnO_2:F (FTO) film was deposited onto the surface of the SRN by ultrasonic spray pyrolysis. Square-shaped patterns with 1 mm^2 area were defined by a photolithography process step to act as gate contact. For SRO-LECs, ~400-nm thick semitransparent n+ polycrystalline silicon (poly) gate was deposited onto the SRO film surface by LPCVD. After a photolithography process step, square-shaped gates of 4 mm^2 area were defined. For SRN/SRO-LECs, ~300-nm thick indium tin oxide (ITO) film was deposited by RF sputtering onto the surface of the films as gate contact. Square-shaped patterns with area of 1 mm^2 were defined by a photolithography process step to act as anode gate contact. Approximately 700-nm thick aluminum (Al) film was evaporated onto the backside of the silicon substrates as cathode contact in all of the LECs. A thermal annealing process at 460°C in N_2 atmosphere for 20 min was used to form the ohmic contact.

The thickness of thermally annealed SRO and SRN films was measured with a Gaertner L117 ellipsometer with a 70° incident laser with wavelength of 632.8 nm and is also shown in **Table 1**. Chemical bonding characteristics was analyzed by means of Fourier transform infra-red spectroscopy (FTIR) with a Brucker V22 equipment in the 4000–350 cm^{-1} range with a resolution of 5 cm^{-1}. The PL spectra were measured with a Fluoromax 3 of Horiba Jobin Yvon. The samples were excited using a 300 nm radiation, and the PL emission signal was collected from 400 to 900 nm with a resolution of 1 nm. The depth analysis profile of thermally annealed SRN, SRO, and SRN/SRO films was analyzed by means of X-ray photoelectron spectroscopy (XPS) Escalab 250Xi of Thermo Scientific equipment, with an Al Kα monochromated source. Current-voltage (I-V) measurements of SRN, SRO, and SRN/SRO-LECs were

http://dx.doi.org/10.5772/64894

performed using a Keithley 4200-SCS parameter analyzer at the same time that the EL was collected with an optical fiber, which was located right on the surface of the device and connected to an Ocean Optics QE-65000 spectrometer.

3. Composition

The composition of SRN and SRO films play an important role in order to understand their luminescence, electrical, and electro-optical properties. In this sense, some techniques such as FTIR and XPS spectroscopies have been used.

3.1. Silicon-rich nitride (SRN) film

The Si-N bonds of SRN films were determined by FTIR measurements. **Figure 1(a)** shows the IR spectra measured from SRN films with $R_N = 5$ (N5), 20 (N20), and 80 (N80) before (B-TA) and after (A-TA) thermal annealing.

IR peaks at 460 and 840 cm^{-1} ascribed to Si-N wagging and stretching modes, respectively, were observed for all samples [35–37]. An IR band appears at 1080 cm^{-1} after thermal annealing, being more evident in the N80 sample. The presence of this peak has been observed before and attributed to a reordering in the films toward a-Si_3N_4 bonding configuration [38, 39]. Nevertheless, it could be related to the Si–O stretching mode due the oxygen incorporation in the samples.

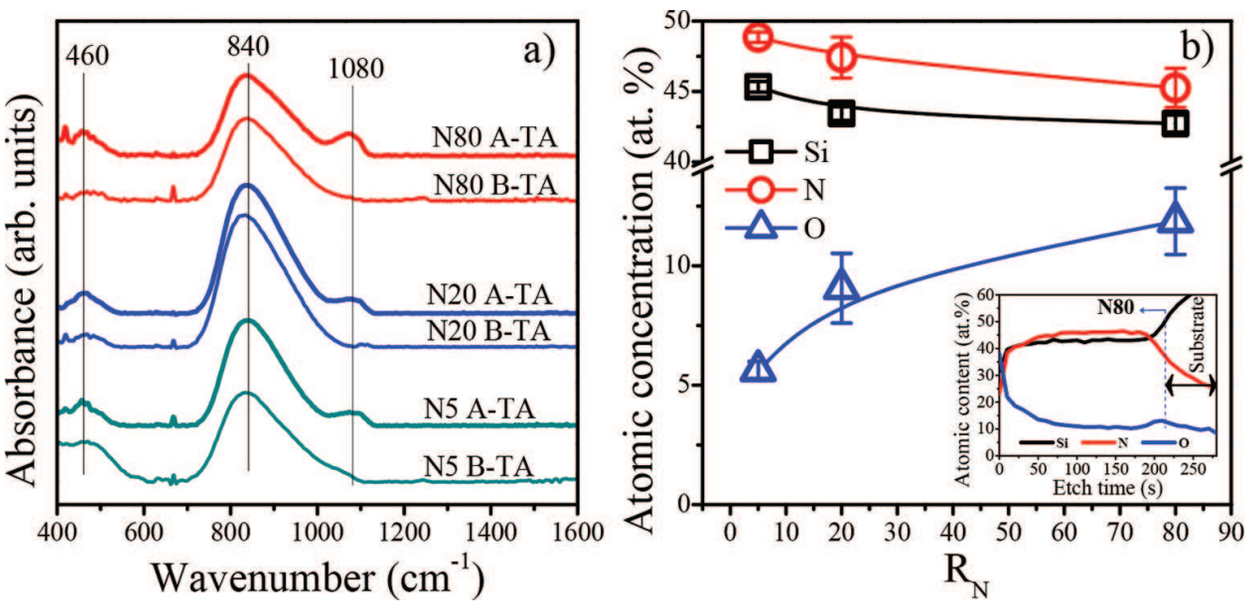

Figure 1. (a) FTIR spectra of SRN films with $R_N = 5$ (N5), 20 (N20) and 80 (N80) before and after thermal annealing, and (b) atomic concentration (at.%) of Si, O, and N as a function of R_N. Inset shows the XPS depth profile of SRN film with $R_N = 80$ (N80). From Cabañas-Tay et al. [34].

In order to comprehend the stoichiometry and the presence of some oxygen into the SRN films, analysis of their composition was performed by means of XPS. **Figure 1(b)** shows information about the chemical composition of the thermally annealed SRN samples. The inset of **Figure 1(b)** exhibits the depth profile composition of the thermally annealed $R_N = 80$ (N80) sample. As can be observed, some oxygen is present at the outmost part of the layer through the film depth, being present mainly at the film surface. This behavior is similar for different R_N, but with different concentrations. **Figure 1(b)** shows the atomic concentration of Si, O, and N as a function of R_N. Mean silicon content values along the layer of 45.55 ± 0.38, 43.58 ± 0.48, and 42.88 ± 1.39 at.% were obtained for the SRN films with $R_N = 5$, 20, and 80, respectively. Moreover, the presence of oxygen increases from 5.6 to 11.8 at.% as the R_N value increases from 5 to 80, respectively.

3.2. Silicon-rich oxide (SRO) film

The Si–O bonds of SRO films were also determined by FTIR measurements. The IR spectra measured from SRO films with *R*o = 20 (M20) and *R*o = 30 (M30) after thermal annealing are shown in **Figure 2(a)**. Typical vibration bands at 460, 810, and 1070 cm^{-1} related to Si–O rocking, Si–O bending, and Si–O stretching modes, respectively, were present in both SRO films [40, 41]. The shoulder from ~1100 to ~1300 cm^{-1} observed in both SRO films has been attributed to Si–O stretching out of phase [42]. It has been reported that this shoulder is less pronounced for the suboxides compared to the stoichiometric oxide [43, 44]. The absorption at 610 cm^{-1} due to unsaturated Si–Si bonds (phonon-phonon interactions) was observed only in M20 (SRO film with higher proportion of silicon precursor) showing the presence of structural imperfections at the SiO_2/silicon nanoparticles (Si-nps) interface [45].

Figure 2(b) exhibits the depth profile composition of the thermally annealed SRO films. Mean silicon content values of 41.85 ± 1.1 and 39.98 ± 0.8 at.% were obtained for the SRO films with

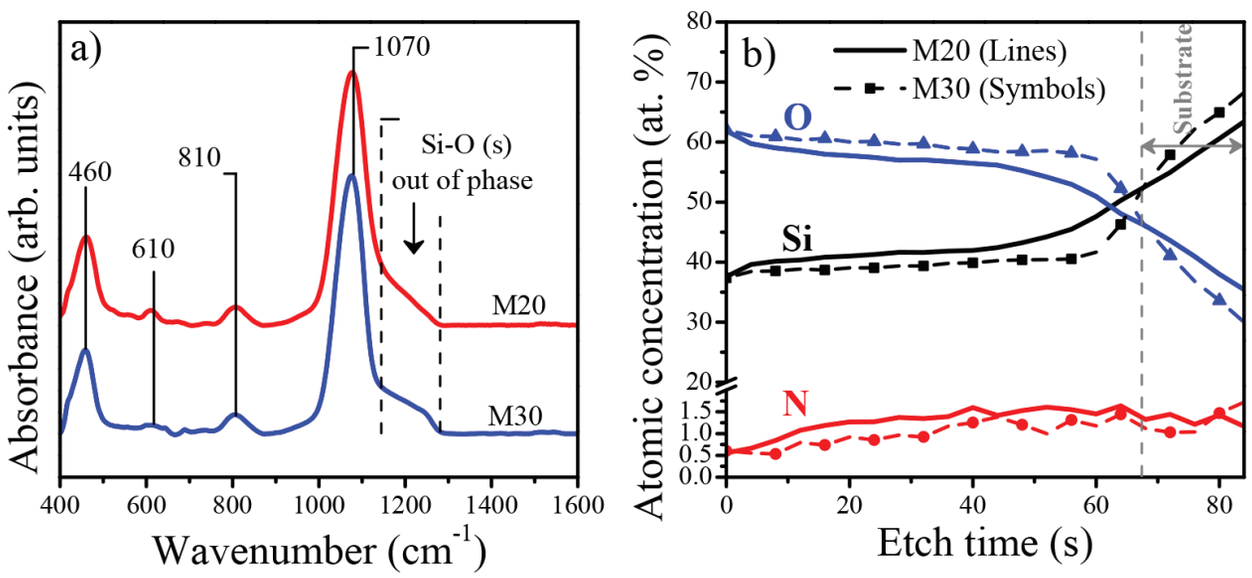

Figure 2. (a) FTIR spectra of SRO films with *R*o = 20 (M20) and 30 (M30) after thermal annealing, and (b) XPS depth profile of SRO films with *R*o = 20 (M20) and 30 (M30).

http://dx.doi.org/10.5772/64894

Ro = 20 (M20) and 30 (M30), respectively. The presence of nitrogen was also observed in both SRO films being slightly more evident for M20. An analysis of the Si2p XPS signal of SRO film with *Ro* = 30 thermally annealed at 1100°C (not showed here) [46] shows that the microstructure of this film is almost a stoichiometric SiO_2 (Si^{4+}) and that the silicon excess is present as Si–O compounds, which could include the neutral oxygen vacancy (NOV) and non-bridging oxygen hole center (NBOHC) defects. As expected by the Si2p XPS signal, crystalline silicon nanoparticles were not observed in this films; however, energy-filtered transmission electron microscopy (EFTEM) analysis has shown (although not clearly) the presence of silicon nanoparticles with a mean size of 1.5 nm and density of ~1.1×10^{12} cm^{-2} as reported in [47, 48]. In fact, it has been reported that a largely disordered system is expected when the size of Si-nps is between 1 and 2 nm. Thus, the small Si-nps are no longer crystalline but amorphous like, as also indicated by theoretical calculations [49, 50]. Then, the dispersed Si atoms in the M30 films are preferentially arranged as very small Si-nps (E'_δ) and some defects like oxygen-deficiency center (ODC) and NBOHC as reported for thin SiOx films (<100 nm) [51].

The presence of the Si^0 peak in the Si2p XPS signal correlates well with the presence of silicon nanocrystal observed by high-resolution transmission electron microscopy (HRTEM, not shown here) in the M20 film. HRTEM reveals Si nanocrystals with an average size (and density) of 2.91 ± 0.40 nm (8.66×10^{11} cm^{-2}) [46].

3.3. Silicon-rich nitride/silicon-rich oxide (SRN/SRO) bilayer

The Si–N and Si–O bonds of SRN/SRO bilayers with *Ro* = 20 (B20) and *Ro* = 30 (B30) were also determined. **Figure 3(a)** shows the FTIR spectra of SRO and SRN/SRO films with *Ro* = 20 (M20 and B20, respectively) after thermal annealing. The IR peak at 820 cm^{-1} observed only in the B20 bilayer is ascribed to Si–N stretching present in SRN films [45]. The intensity of a shoulder

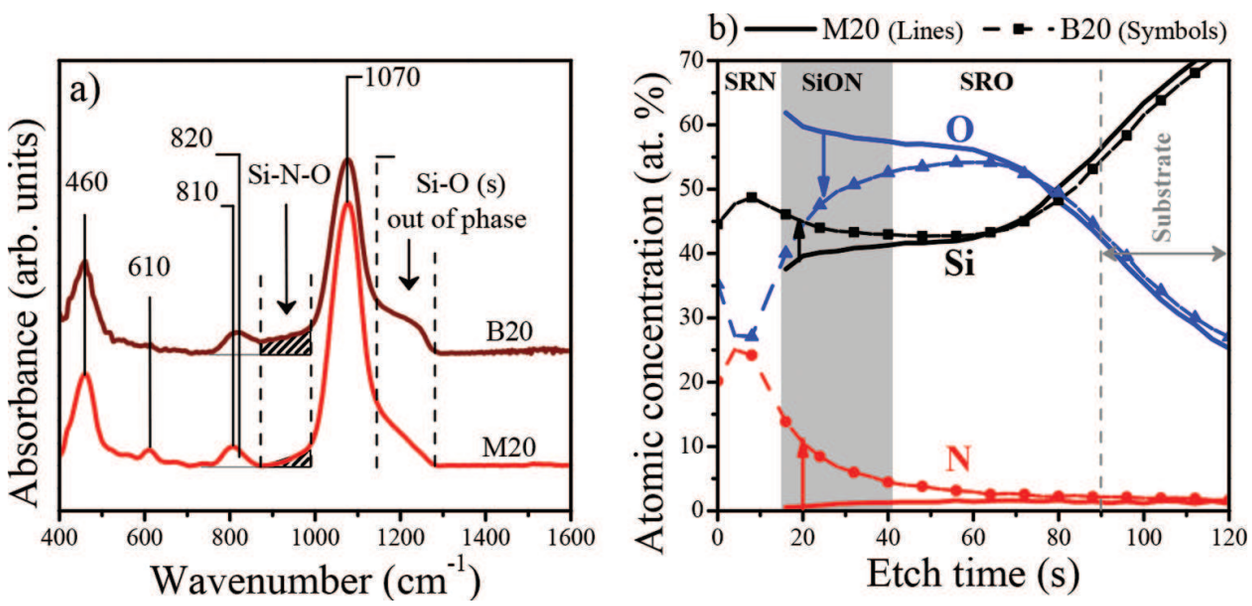

Figure 3. (a) FTIR spectra of SRO and SRN/SRO films with *Ro* = 20 (M20 and B20, respectively) after thermal annealing, and (b) XPS depth profile of SRO and SRN/SRO films with *Ro* = 20 (M20 and B30, respectively) after thermal annealing.

(shadow area) from 900 to 1000 cm^{-1} increased when the B20 bilayer was formed, and it was attributed to the formation of Si–N–O bonds in silicon oxynitride [45].

As shown in **Figure 3(a)**, the shoulder from ~1100 to ~1300 cm^{-1} was observed in both samples (M20 and B20) and it was attributed to Si–O stretching out of phase [42]. The IR peak at 610 cm^{-1} observed in the SRO monolayer (M20) disappeared for the bilayer (B20) and it could be related to the nitrogen incorporation within the SRO that creates Si–N–O–Si bridges. The presence of these bridges decreased the quantity of strained bonds and Si dangling bonds at the SiO_2/Si-np interface [45]. The SRN/SRO film with $Ro = 30$ (B30) showed the same IR peaks than the B20 bilayer, except for the 610 cm^{-1} IR peak.

Figure 3(b) showed the depth profile composition of the thermally annealed SRO monolayer and SRN/SRO bilayer, both with $Ro = 20$ (M20 and B20, respectively). The average Si content within the SRO monolayer was about 41.85 ± 1.1 at.%. When the SRN/SRO bilayer was formed, the oxide-nitride interface became an imprecise oxynitride (SiON) layer almost for 30 s etching time (shadow area in **Figure 3(b)**). In that region, a gradual increasing of both nitrogen and silicon was observed toward the interface. The average Si content slightly increased up to ~43.21 ± 0.7 at.% in the SRO layer, whereas the oxygen content in the SRO film was reduced from 56.78 ± 1.3 to 53.08 ± 1.0 at.%. The Si, O, and N diffusion could be enhanced by the high annealing temperature. This is supported by two facts: first, the presence of a nitrogen concentration within the oxide layer which goes from 2 to 10%, and second, the oxygen presence in the nitride layer (~25%). The nitrogen content inside of the SRO in the SRN/SRO bilayer structure could modify its optical and structural properties. It has been reported that the nitrogen hinder the diffusion of Si atoms and prevents the phase separation in the amorphous SiOx:N films [52]. Thus, the mobility of the Si atoms is smaller and the growth of the Si-nps during the thermal diffusion process is reduced, giving as a result smaller Si-nps. A similar behavior was observed for the B30 bilayer, but with different concentration.

4. Photoluminescence

4.1. Silicon-rich nitride (SRN) film

The PL spectra of SRN films before and after thermal annealing are shown in **Figure 4**. The PL intensity was normalized to the thickness of each SRN film. The as-deposited SRN film with $R_N = 80$ (N80) emit a broad PL band with the main peak at 490 nm, as shown in **Figure 4(a)**. As the R_N value decreases, the PL emission band becomes narrower and shifts to a higher wavelength reaching 590 nm for $R_N = 5$ (N5, higher silicon excess) but with a lower intensity.

The PL band of the SRN films blueshifts after thermal annealing, particularly for $R_N = 80$ where the main band shifts from 490 to 420 nm, as shown in **Figure 4(b)**. It is well known that the silicon excess in silicon-rich dielectrics agglomerates forming Si-nps after high temperature annealing, resulting in a redshift of the PL band due to the quantum confinement effects [53–57]. However, contrary to this assumption, in this work, the PL blueshifts after the annealing, as shown in **Figure 4(b)**. This effect has been observed before and it has been ascribed to compositional-dependent changes in the concentration of defect states within the samples [58].

http://dx.doi.org/10.5772/64894

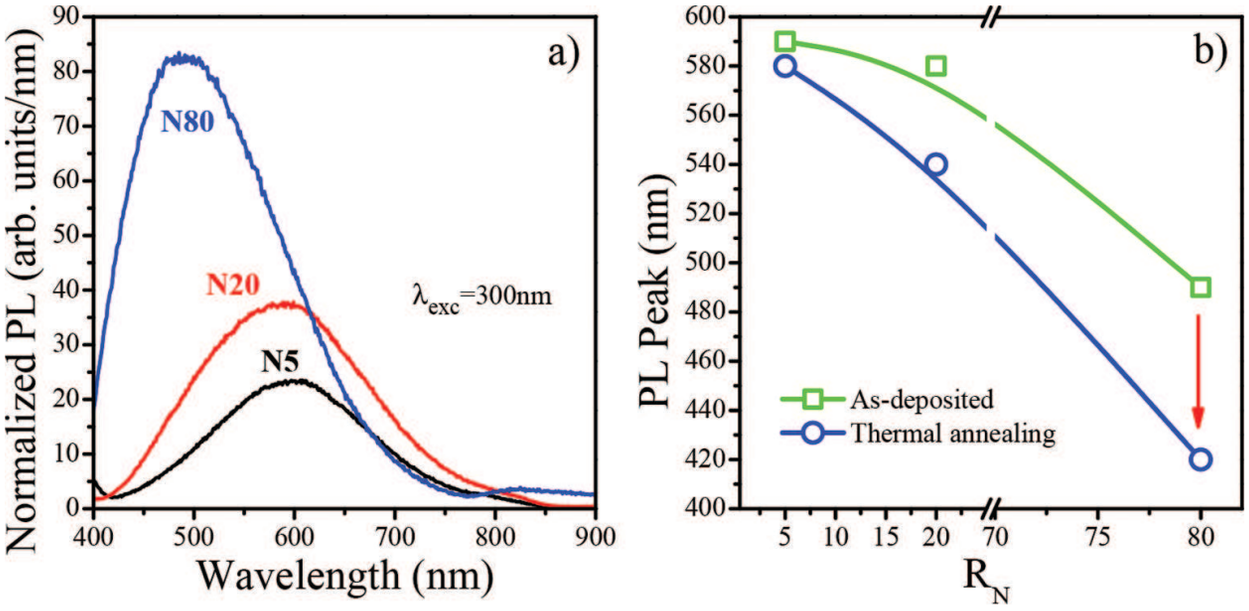

Figure 4. (a) Normalized PL spectra of as-deposited, and (b) maximum PL peak position before and after thermally annealed, SRN films with $R_N = 5$ (N5), 20 (N20), and 80 (N80). Lines are plotted as an eye-guide. From Cabañas-Tay et al. [34].

Therefore, defects are created rather than Si-nps, after thermal annealing. Moreover, due to the low diffusivity of silicon atoms in Si_3N_4, a high Si content (>52 at.%) is needed to form Si-nps [59, 60]. Because of the low Si content present in the SRN films from this work (<46 at.%), as shown above in the XPS results, these films can be explained as a sub-stoichiometric nitride with structural defects, as reported in the study of Cabañas-Tay et al. [34].

PL bands between 380 and 600 nm (2.0–3.2 eV) have been observed before in SRN films, and they have been ascribed to the radiative recombination of carriers in band tail states, which are related to defect energy levels within the gap of amorphous silicon nitride [61–64]. Therefore, the PL bands emitted by the SRN films from this work can be explained by the excitation of different defects as discussed in the study of Cabañas-Tay et al. [34]. As observed in **Figure 4(a)**, the as-deposited SRN films emit at 590, 580, and 490 nm, whereas the thermally annealed films emit at 580, 540, and 420 nm for R_N of 5, 20, and 80, respectively. PL emission bands observed at 580–590 nm (~2.1 eV) have been related to electronic transitions from the conduction band minimum (CBM) to K^0 centers located near of the mid-gap, the emission band at 540 nm (~2.3 eV) is related to electronic transition from the K^0 centers to $=N^-$ centers located near of the valence band maximum (VBM), and the emission band at 420 nm (~2.9 eV) has been related to electronic transitions from the K^0 centers to VBM. Hence, the PL bands observed in this work could have a similar origin, as discussed in the study of Cabañas-Tay et al. [34].

Some studies have shown that electronic transition related with K^0 centers to =Si–O–Si states are observed when oxygen is incorporated in the SRN film [65, 66]. The presence of oxygen in SRN films creates a gap state of Si–O above the VBM, giving rise to the 485 nm (~2.55 eV) emission. The XPS analysis demonstrated that SRN films contain oxygen, being the higher concentration for $R_N = 80$ (11.8 at.%). Therefore, the PL emission band at 490 nm (~2.53 eV)

observed in the as-deposited sample with $R_N = 80$ could be related to the electronic transition from the K^0 centers to =Si–O–Si states.

In summary, the analysis of the PL emission observed in the SRN films before and after thermal annealing indicates that it could be mainly originated from the radiative recombination via luminescent Si dangling bonds, N dangling bonds, and Si–O bonds existing in the silicon nitride matrix.

4.2. Silicon-rich oxide (SRO) film

Figure 5 shows the normalized PL spectra of SRO films before and after thermal annealing. The as-deposited SRO film with *R*o = 30 (M30) emits a broad PL band with the main peak at 460 nm. After thermal annealing, the PL emission band becomes narrower and redshifts reaching 690 nm, as shown in **Figure 5(a)**. As the *R*o value decreases, the PL emission band becomes wider and shifts to a higher wavelength reaching 660 nm for *R*o = 20 (M20, higher silicon excess), as shown in **Figure 5(b)**. After thermal annealing, the PL of M20 redshifts, reaching 740 nm.

The PL emitted by M30 exhibit a significant redshift of the main peak after thermal annealing as shown in **Figure 5(a)**. Nevertheless, when the silicon content is increased (M20), the PL band appears mainly at the red side of the spectrum. The redshift of the main PL peak (after thermal annealing) has been widely observed and ascribed to the agglomeration of silicon excess and a subsequent silicon nanoparticle formation as a result of thermal annealing process [67–71]. Nevertheless, some point defects are also present within the SRO films. It is widely accepted that violet-blue (400–460 nm), green (520), and even red (630) emission bands, obtained from the deconvolution of the PL spectrum [72], can be related with oxygen

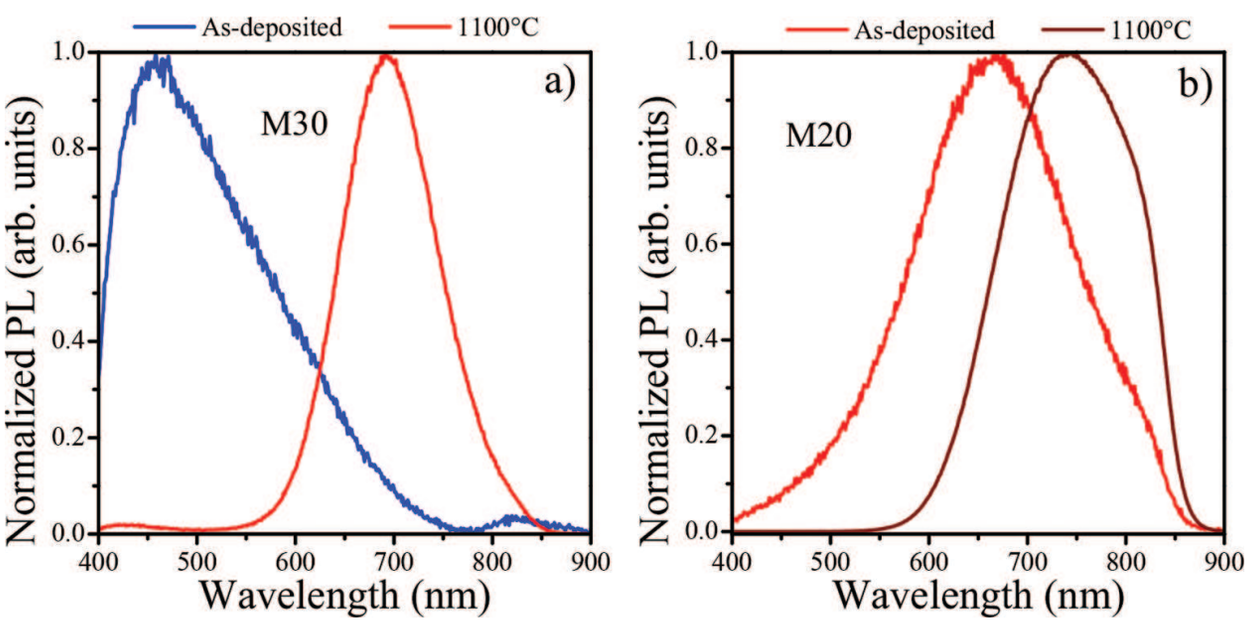

Figure 5. Normalized PL spectra of SRO monolayer (a) with *R*o = 30 (M30) and (b) *R*o = 20 (M20) before and after thermal annealing. From Palacios-Huerta et al. [46].

defect centers (ODC), E'_{δ} (Si↑Si=Si) and NBOHC defects, respectively [67–71]. The E'_{δ} center is one of the at least four different E′ centers [43], which comprises an unpaired spin delocalized over five silicon atoms and suggest the presence of very small Si-nps in the films.

4.3. Silicon-rich nitride/silicon-rich oxide (SRN/SRO) bilayers

In previous studies, it has been reported that the combination of Si_3N_4/SRO structure improves luminescent emission properties [73, 74]. Previous studies have also shown that a Si_3N_4-SRO bilayer structure improves the operation of light-emitting devices, such as a reduced leakage current, a reduced electric field on the oxide layer, and results an improvement in efficiency and a longer device life [73–76]. In this chapter, the effect of a SRN film on a SRO film (SRN/SRO bilayers) on their optical properties is analyzed. SRN films, deposited by LPCVD with $R_N = 80$ (N80), show luminescence in the blue region, while the SRO films emit in the red region, as observed in **Figures 4** and **5**, respectively. Therefore, a combination of SRN with $R_N = 80$ and SRO films could allow reaching a broad emission spectrum.

Figure 6 shows the PL spectra of SRN/SRO bilayers with *R*o = 20 (B20) and 30 (B30) after thermal annealing. The emission spectra of the SRN (N80) and SRO monolayer films with *R*o = 20 (M20) and 30 (M30) are shown as references, respectively. The emission spectra of the samples were normalized to the SRO thickness. Each PL spectrum of SRN and SRO

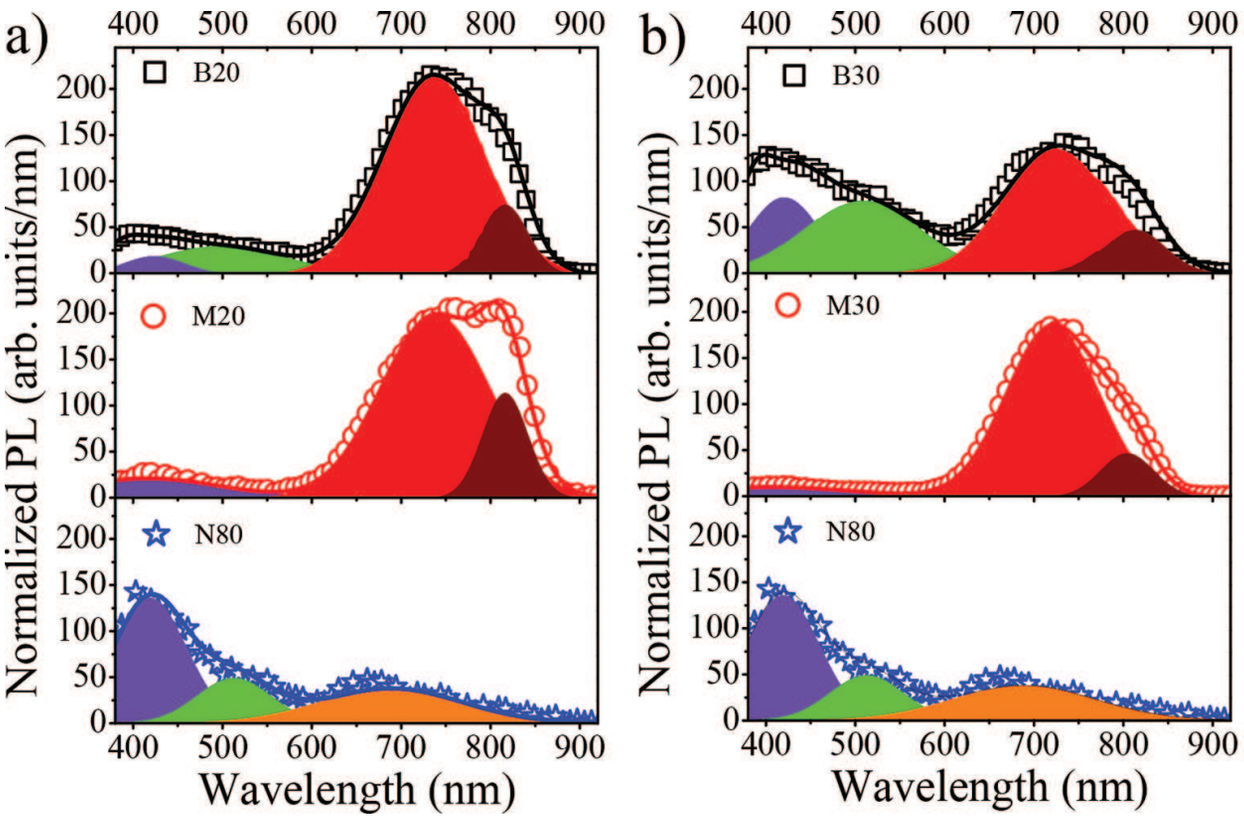

Figure 6. Normalized PL spectra after thermal annealing of (a) SRN/SRO film with *R*o = 20 (B20), SRN film with $R_N = 80$ (N80), and SRO with *R*o = 20 (M20), and (b) SRN/SRO film with *R*o = 30 (B30), SRN film with $R_N = 80$ (N80), and SRO with *R*o = 30 (M30).

monolayers was fitted three Gaussian, while four Gaussians were used to fit the PL spectrum of the SRO/SRN bilayer.

For the SRN film (N80), PL bands at about ~420, 505, and 680 nm were identified, which are related to electronic transitions from the K^0 centers to the VBM, K^0 centers to =Si–O–Si, and states of defects nitrogen (N^0_2), respectively [64]. For the SRO film with *R*o = 20 (M20), PL bands at ~420, 735, and 820 nm were identified and have been widely related to weak oxygen bond (WOB) defects, interactions that take place at the Si-np/SiOx interface, and quantum confinement in silicon nanocrystals, respectively [72]. The PL spectrum of the SRN/SRO bilayer with *R*o = 20 (B20) exhibits the same PL bands of the SRO films at ~420, ~735, and 812 nm, but with an additional band at ~505 nm (green band), which is related to transitions from K^0 centers to =Si–O–Si featured of the SRN film, as shown in **Figure 6(a)**.

As observed in **Figure 6(b)**, the SRO monolayer with *R*o = 30 (M30) exhibits PL bands at ~420, 720, and 805 nm, which have been also linked to WOB defects, interactions that take place at the Si-nps/SiOx interface, and silicon nanocrystals (Si-ncs) through quantum confinement, respectively [72]. The PL spectrum of the SRN/SRO with *R*o = 30 (B30) is composed by the same luminescent bands than that observed in the bilayer with *R*o = 20 (B20), but with an increased intensity of the bands at ~420 and ~505 nm related with transitions from K^0 centers to VBM (violet band), transitions from K^0 centers to =Si–O–Si (green band), respectively.

In summary, it is observed that the emission intensity in the blue and green bands (~420 and 505 nm) is improved when a SRN/SRO bilayer is formed compared to SRO monolayers, being higher when a *R*o = 30 (B30) is used. The XPS results show a diffusion of oxygen from the SRO layer to the SRN layer and nitrogen from the SRN layer to the SRO layer during SRN deposition (onto SRO layer). Therefore, some defects could be passivated into the SRO layer and others generated into the SRN layer like WOB or =Si–O–Si defects.

5. Electroluminescence

SRN, SRO, and SRN/SRO films exhibit intense and visible photoluminescence. In this section, luminescent characteristics of the samples are present but under electrical excitation.

5.1. Silicon-rich nitride (SRN)-LECs

Figure 7 shows the EL spectra of the light emitting capacitors using the as-deposited SRN film with $R_N = 20$ as an active dielectric layer at different injected currents. At forward bias (FB) (positive voltage to FTO contact respect to Si substrate), the SRN-LEC shows a broad spectrum with the maximum emission centered at around 580 nm, and it remains at the same wavelengths for different voltages as shown in **Figure 7(a)**. This luminescence has been reported as a characteristic behavior of defect-related EL [67]. In fact, the luminescent properties of SRN films in this chapter are related to the presence of defects. Therefore, the EL in SRN-LECs may originate from the same electronic transitions of the CBM to K^0 centers,

http://dx.doi.org/10.5772/64894

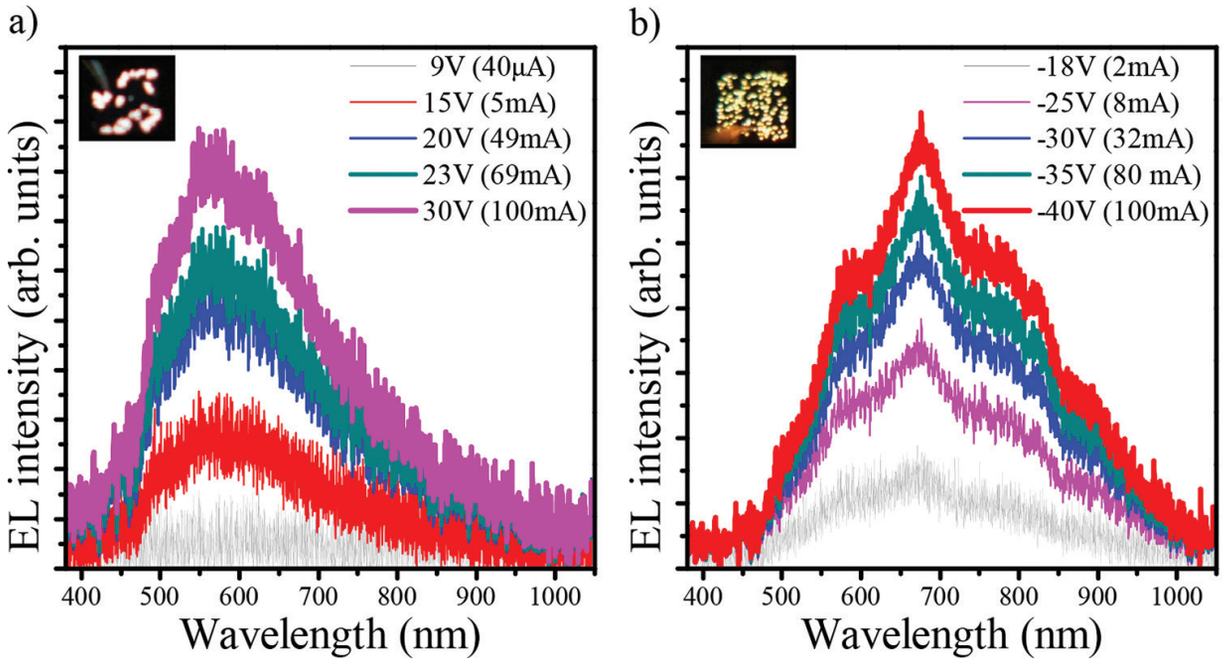

Figure 7. EL spectra of the as-deposited SRN LEC with $R_N = 20$ for different injected currents at (a) forward bias and (b) reverse bias. In the inset, pictures for the device with 100 mA of injected current for each bias. FTO was used as gate electrode. From Cabañas-Tay et al. [34].

as observed in PL [77, 78]. This behavior is similar for all SRN films in both as-deposited and after thermal annealing, as reported in the study of Cabañas-Tay et al. [34].

On the other hand, at reverse bias (RB), the EL spectrum changes and now three main emission bands are observed at around 600, 680, and 780 nm, as observed in **Figure 7(b)**. Namely, the maximum emission band blueshifts when the polarity is changed from RB to FB. The EL bands at 600, 680, and 780 nm also remains at the same wavelength when the voltage is increased indicating the EL emission is also produced by defects. These EL bands have been ascribed to electronic transitions from the K^0 centers to valence band tail states [58, 77]. The EL emission for all the SRN-LECs in both polarities is through shine dots as shown in the inset of **Figure 7(a)** and **(b)**. The device's area is covered with more shine dots when the current increases. The EL emission composed by shining spots is attributed to the formation of a finite number of preferential conductive paths within the SRN films, which connect the top and bottom electrodes, as discussed in the study of Cabañas-Tay et al. [34].

Negligible spectral shift is observed between the EL at forward bias and PL spectra of SRN films with $R_N = 5$ and 20 before and after thermal annealing, indicating that both PL and EL emissions are originated from the same radiative centers [34]. Nevertheless, a long spectral shift is observed for the SRN films with $R_N = 80$ (before and after thermal annealing). This behavior was explained as a significant smaller electrical pumping of electrons allowing the holes to relax to the lowest defect states before recombining. For the EL at RB, a similar behavior is presented but the electrical pumping of electrons is slightly improved allowing only few of the holes to relax to the lowest defect states before recombining [34].

5.2. Silicon-rich oxide (SRO)-LECs

The presence of defects including the Si-nps, either crystalline or amorphous, and their density and size in silicon-rich dielectric materials affect clearly the current transport, and therefore the EL, as in the SRO case. **Figure 8** shows J-E curves of SRO-LECs with *R*o = 30 and 20; samples were thermally annealed at 1100°C. SRO-LECs are forwardly biased (accumulation mode) considering the substrate as reference.

SRO-LECs with *R*o = 30 (M30) films show a high current state (HCS) at low electric fields, then after the applied voltage increased, the current was switched to an LCS, as shown in **Figure 8**. This behavior was observed by our group before in SRO films with *R*o =30, and it was related to the creation and annihilation of preferential conductive paths generated possibly by adjacent stable Si-nps and unstable silicon nanoclusters (Si-ncls) through structural changes and by the possible creation of defects (breaking off Si–Si bonds) [70, 79, 80]. Indeed, a clear correlation between current jumps/drops and EL dots appearing/disappearing on the LEC surface was observed [70, 79, 80]. This RS behavior is independent on the thermal annealing temperature [46]. Recent studies regarding the same electrical RS behavior in SRO films was observed and related with a conductive filament formed by Si-nps [81–84], which undergoes structural changes through a crystallization and amorphization process of the Si-nps, as discussed in [82]. Such observations are in agreement with the presented asseverations about the behavior of the SRO with *R*o = 30 (M30)-based LECs.

Once the current fluctuations disappear, through the electrical annealing, the current behavior stabilized (see I–V curve marked as M30-after in dark blue line, **Figure 8**) and EL on the whole area (WA EL) was observed at higher electric fields. On the other hand, the electrical behavior of SRO-LEC with *R*o = 20 (M20) did not show current fluctuations. The latter could

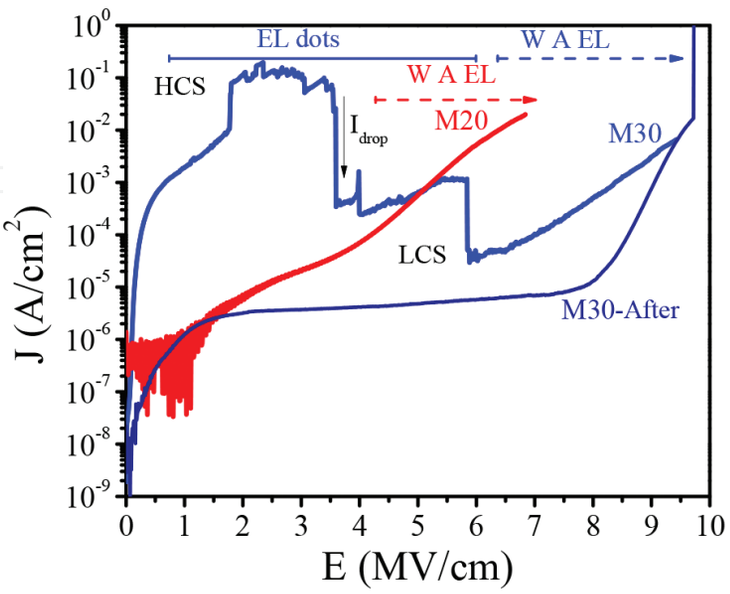

Figure 8. J-E curve of SRO-LECs with *R*o = 20 (M20) and 30 (M30) thermally annealed at 1100°C. From Palacios-Huerta et al. [46].

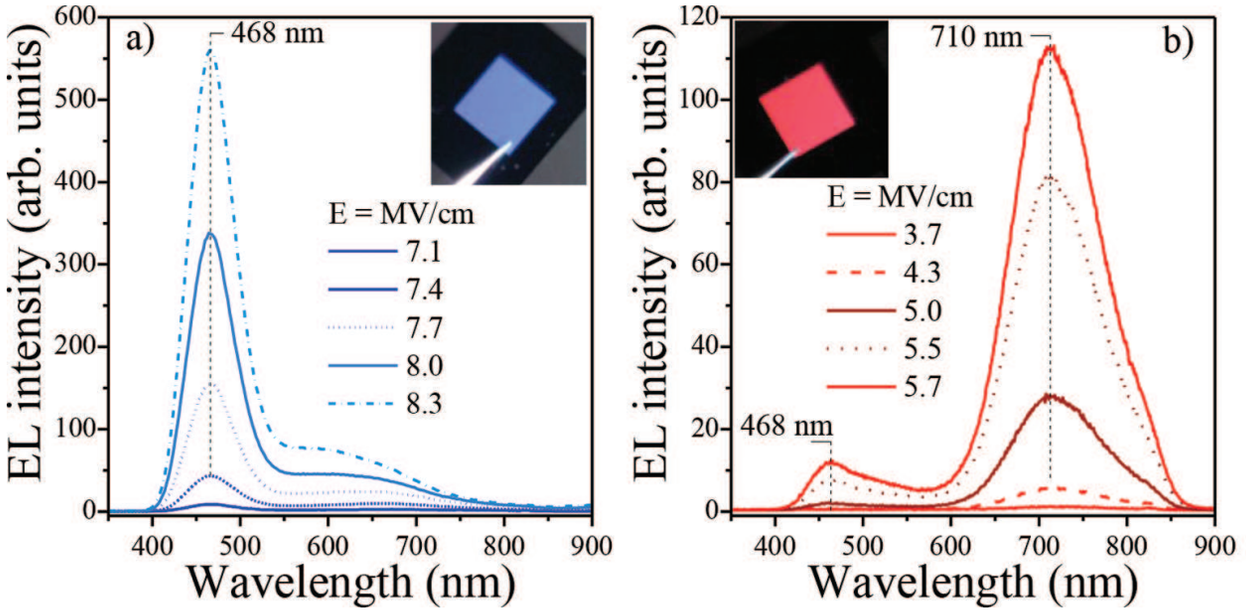

Figure 9. EL spectra and images of SRO-LECs with (a) *Ro* = 20 (M20) and (b) 30 (M30) annealed at 1100°C. Semitransparent n+ polycrystalline silicon was used as gate electrode. From Palacios-Huerta et al. [46].

be related to the presence of well-separated and crystalline silicon nanoparticles, mainly on the density of Si-nps, as shown by transmission electron microscopy (TEM) analysis [46]. Therefore, a uniform network of conductive paths becomes possible as the Si-nps density increases, allowing a uniform charge flow through the whole capacitor area.

Figure 9 shows the EL spectra from the SRO-LECs. Blue EL in the whole area was observed with *Ro* = 30 (M30) only after the current drop. The main EL peak remains at 468 nm when the electric field increases, as observed in **Figure 9(a)**. When the silicon content is increased (*Ro* = 20), the LECs emit a broad EL spectrum in the red region, as observed in **Figure 9(b)**. The EL peak is placed at 710 nm. This value is blueshifted with respect to the value found in PL at 740 nm. Differences in the PL and EL peak wavelength have been related to the transmittance of the top electrode, which influences the real light emission from the active layer [85]. Indeed, the process of carrier injection and the several transport mechanism taking place through the active luminescent materials produces a complicated understanding of the EL process, as compared to the PL one [86]. Nevertheless, both EL and PL spectra appear in the same red region, which could indicate that the emission is originated by the same radiative centers. Images of LECs are shown as insets in **Figure 9**. As can be observed, the LEC devices emit an intense whole area EL.

5.3. Silicon-rich nitride/silicon-rich oxide (SRN/SRO)-LECs

Figure 10 shows the J(E) characteristic and the EL spectra of SRN/SRO-LECs at forward bias considering the substrate like reference. SRN/SRO-LECs show a high current state (HCS) at low electric fields, and then after the applied voltage increases, the current is switched to a LCS, as shown in **Figure 10(a)**. The resistive switching in the B20 bilayer occurs at a lower electric field (~2 MV/cm) compared to the B30 bilayer. When SRN/SRO-LECs, both with *Ro* = 20

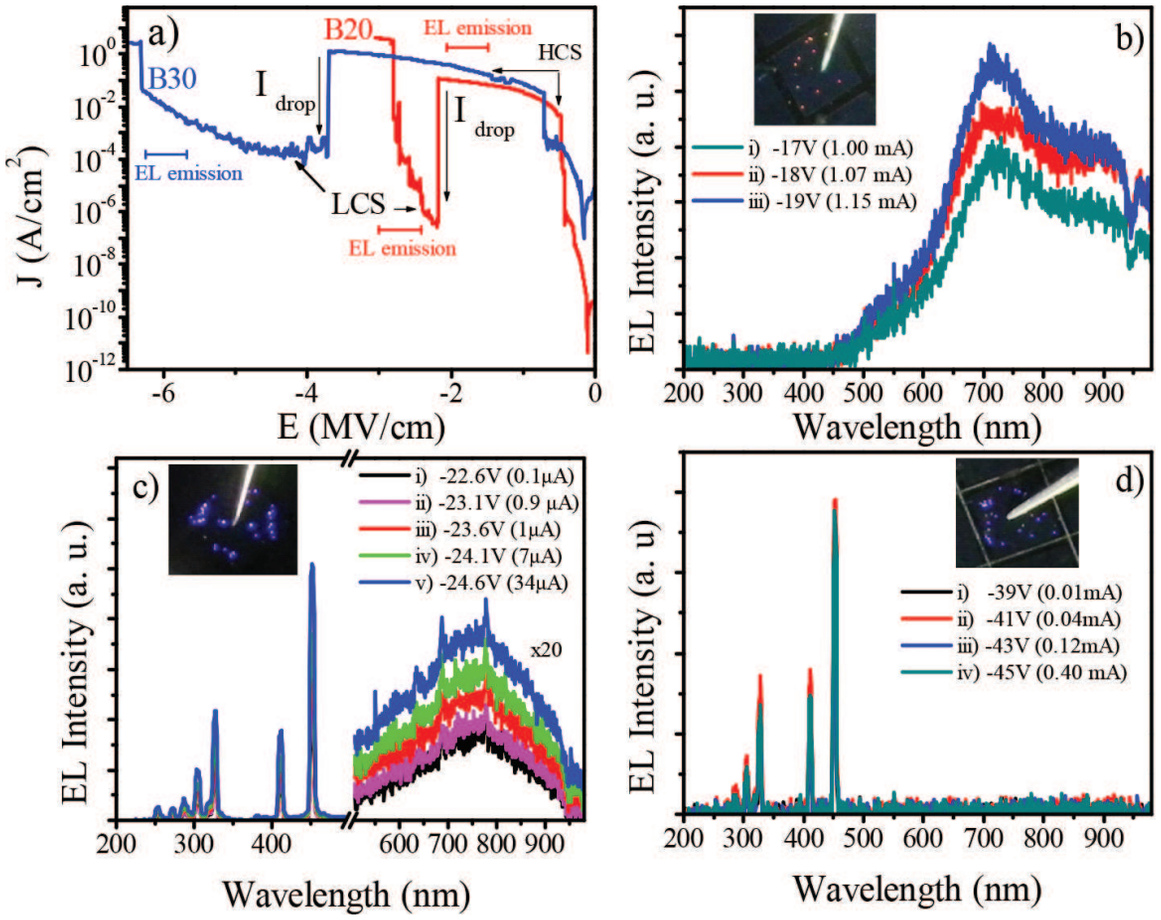

Figure 10. (a) J-E curve of SRN/SRO-LECs with *Ro* = 20 (B20) and 30 (B30) and EL spectra of SRN/SRO LECs at forward bias for different currents applied with (b) *Ro* = 20 (B20) in the HCS, (c) *Ro* = 20 (B20) in the LCS, and (d) *Ro* = 30 (B30) in the LCS. Inset of each graph are shown photographs of the LEC. ITO was used as gate contact.

(B20) and *Ro* = 30 (B30), are in the HCS (<20V), a broad spectrum with the maximum emission centered at about 730 nm and a shoulder at ~900 nm is observed. The 730 nm emission increases as the voltage also increases, as observed in **Figure 10(b)**. Nevertheless, first the shoulder at 900 nm increases its intensity when the voltage is between −17 and −18 V and then remains at the same value for larger voltages. As we can see in **Figure 10(b)**, the EL is observed as randomly scattered luminescent spots (mainly red) over the entire LEC surface. The spectrum exhibits that the EL emission follows the PL, showing that the emission is caused by the same luminescent centers.

After current switching, in the LCS (>20V), the EL spectra changes, as observed in **Figure 10(c)**. Also, a narrow (width of 7 ± 0.6 nm) and highly intense UV EL peaks appear at ~250, 270, 285, 305, 325, and 415 nm. A narrow blue EL peak with the highest intensity is observed at ~450 nm. All EL peaks remain at the same wavelength as the current increases. The red EL band observed in the HCS is still present at the LCS, but with a slight redshift and with a low intensity. The emission intensity of the blue EL is about 20 times higher than the red emission. The EL emission is observed as luminescent blue-violet dots randomly distributed on the surface of the contact, as shown in the insets of **Figure 10(c)**.

Figure 10(d) shows the EL emission of the SRN/SRO-LEC with *R*o = 30 (B30) in the range of LCS (>35V). The same narrow and highly intense UV EL peaks at ~250, 270, 285, 305, 325, 415, and 450 nm with an average width of 7 ± 0.6 nm are also observed in these devices. Nevertheless, these LECs do not show EL emission in the red-near infrared region.

Four narrow UV EL peaks have been reported at 293.78, 316.10, 403.07, and 444.82 nm, with an average width at half peak of 4 nm, in ITO/Y_2O_3/Ag EL devices. This emission was attributed to the characteristic radiation of indium ions [87]. However, as the best of our knowledge, narrow UV EL peaks in silicon rich dielectric materials have not been reported before. The most intense EL peaks emitted by the present SRN/SRO-LECS (~305, 325, 415, and 450 nm) are very similar to those obtained in reference [87], but displaced ~10 nm toward longer wavelengths. Thus, they could have a similar origin; however, a deeper analysis of these narrow emission bands needs to be done.

6. Conduction mechanisms

The origin of the EL emission from the SRO, SRN, and SRN/SRO-LECs can be determined by identifying the charge transport mechanism that takes place within the different silicon-rich dielectric materials as discussed below.

6.1. Silicon-rich nitride (SRN)-LECs

Figure 11 shows the J(E) dependency for the SRN-LECs with R_N = 5, 20, and 80. The conduction mechanism of the carriers in the SRN films was studied by analyzing the different reported mechanism including P-F conduction [88, 89], TAT [90], and space charge limited current (SCLC) [91]. As observed in **Figure 11**, the TAT mechanism is dominating the carrier transport at both forward and reverse bias, and it can be ascribed to the defect states generated during the SRN deposition. A model based on the trap-assisted tunneling carrier transport is shown with the EL radiative recombination process in the reference [34].

6.2. Silicon-rich oxide (SRO)-LECs

Figure 12 shows the experimental J-E data from SRO-LECs with *R*o = 20 and 30 fitted to the carrier transport mechanisms including Poole-Frenkel (P-F) conduction [88, 89] and trap-assisted tunneling (TAT) [90]. As can be observed, the TAT conduction mechanism predominates in the SRO-LEC with *R*o = 30 (M30).

The trap energy was estimated to be $\phi_t \cong 1.75$ eV, if a uniformly distributed trap concentration is assumed. It is worth to mention that these trap energy levels correlates well with the one obtained for Er-doped SRO/SiO_2 superlattice (2.1 eV) and Er-doped SiO_2 (1.9 eV), which are assumed to be deep traps inherent to the SiO_2 [92] possibly neutral oxygen vacancy [93]. Mehonic et al. have reported that the barrier height of the trap is modified by the concentration of oxygen vacancies in the connecting tissue; lower barrier heights correspond to a higher concentration of oxygen vacancies, which defines the device resistance [84]. Moreover, it has been reported that a poor quality of nanocrystalline composite material (formed by Si

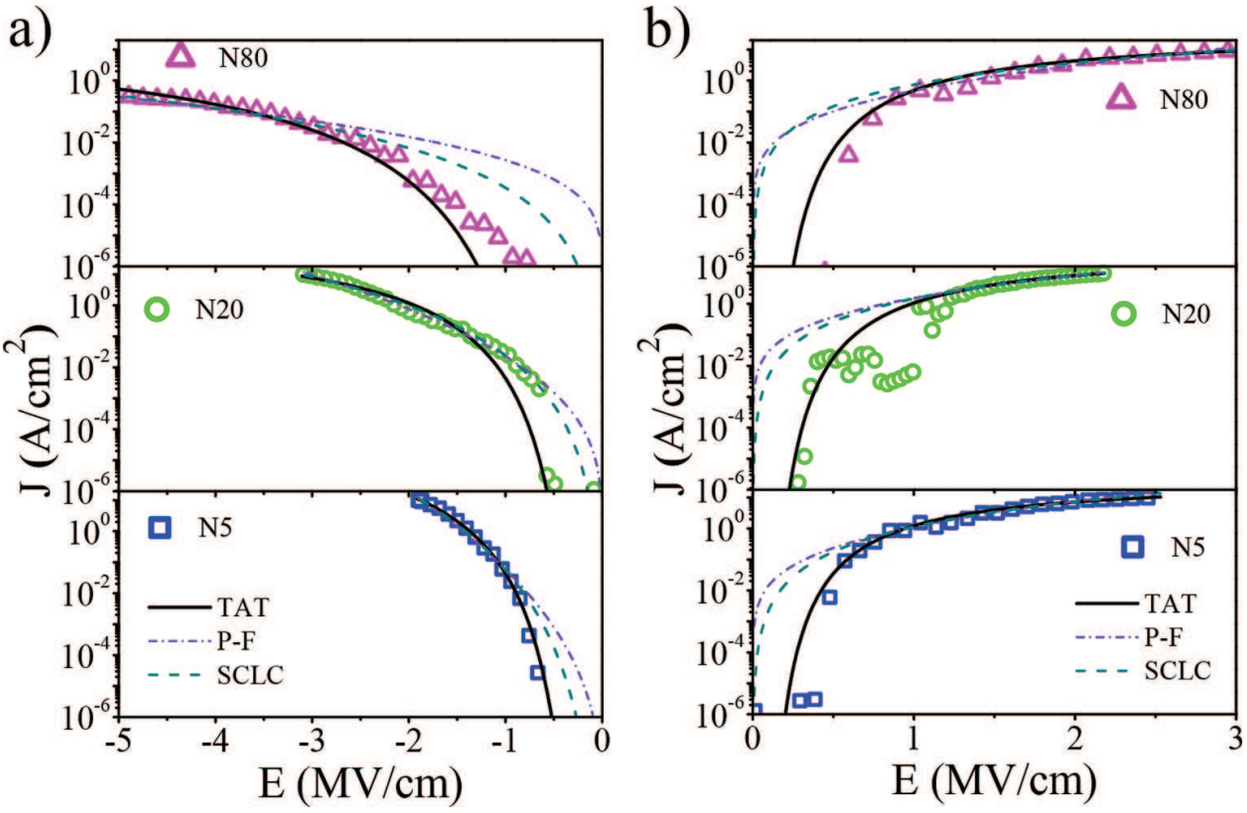

Figure 11. J-E characteristic and conduction mechanism fitting of SRN-LECs with R_N = 5 (N5), 20 (N20), and 80 (N80) after thermal annealing at: (a) reverse bias (RB) and (b) forward bias (FB). Symbols are the experimental current data, black line represents the TAT conduction, green dash line SCLC, and violet dash dot line the Poole-Frenkel conduction. From Cabañas-Tay et al. [34].

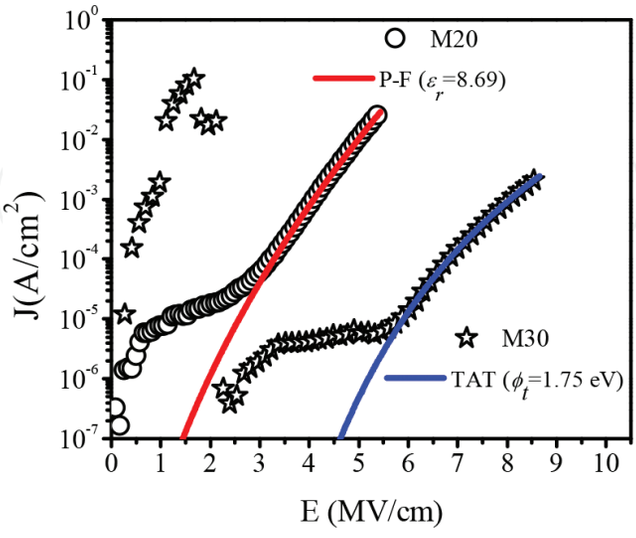

Figure 12. J-E characteristic and conduction mechanism fitting of SRO-LECs with *Ro* = 30 (M30) and *Ro* = 20 (M20). Red line represents the TAT conduction and blue line the Poole-Frenkel conduction. Symbols are the experimental data. From Palacios-Huerta et al. [46].

http://dx.doi.org/10.5772/64894

nanocrystals and SiOx) yields parasitic current paths, while low density of nanocrystals turns difficult the direct charge injection into the nanocrystals [94]. A similar behavior is obtained for SRO-LECs with *Ro* = 30 (M30), where the annihilation of conductive paths, created by adjacent stable Si-nps and unstable silicon nanoclusters (Si-ncls), produce structural changes including the possible creation of defects. Then, it can be assumed that M30 films exhibit a poor quality of the silicon oxide resulting from the phase separation and the low silicon content. This behavior is well correlated to the blue EL emission observed in the M30-based LECs.

On other hand, the P-F conduction fits well the charge transport in SRO-LECs with *Ro* = 20 (M20), as observed in **Figure 12**. A relative permittivity (ε_r) value of 9.16 was obtained from the P-F fit for M20, which is closer to the relative permittivity of silicon ($\varepsilon_{Si} = 11.9$), similar to other reports [92]. Relatively high permittivity values are a good indication of the large amount of silicon present as Si-nps within the M20 films. Moreover, the Si-nps size calculated by using the P-F estimate relative permittivity are very close to that obtained through the TEM analysis, as reported in [46].

6.3. Silicon-rich nitride/silicon-rich oxide (SRN/SRO)-LECs

When the SRN/SRO bilayer structure is used as active layer in LECs, several charge transport mechanisms are present, as observed in **Figure 13**. For the SRN/SRO-LEC with *Ro* = 20 (B20), and in the HCS where red EL emission is observed, the hopping tunneling is the predominant mechanism (pink line), as shown in **Figure 13**(a).

The average distance between traps (*a*) was estimated to be about 0.25 nm. When the current switches to the low conduction state, the tunneling mechanism changes, then the P-F conduction

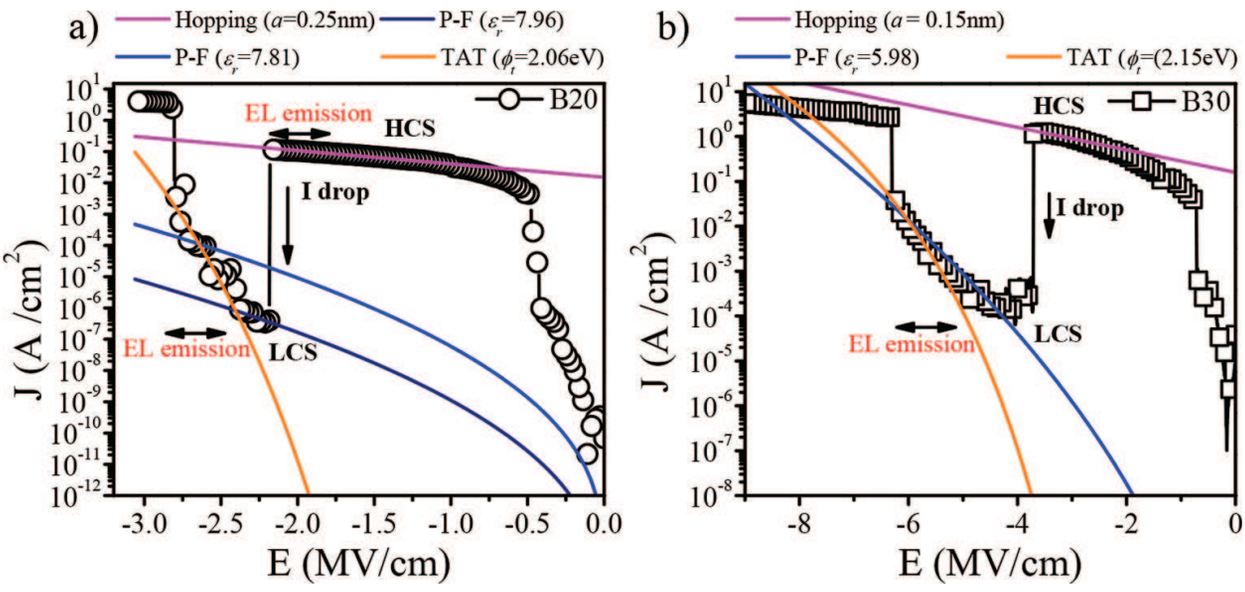

Figure 13. J-E characteristic and conduction mechanism fitting of SRN/SRO-LECs with (a) *Ro* = 20 (B20) and (b) *Ro* = 30 (B30) thermally annealed at 1100°C. Pink line represents the hopping conduction, orange line the TAT conduction, and blue lines the Poole-Frenkel conduction. Symbols are the experimental data.

dominates (dark blue line). The dielectric constant (ε_r) obtained by the P-F fit was about 7.96. However, when the deep UV EL emission starts, the conduction transport is dominated by two different mechanisms: TAT (orange line) and P-F (blue line). In this region, the traps depth obtained by the TAT fit was about 2.06 eV, and the dielectric constant (ε_r) obtained by the P-F fit was about 7.81.

The SRN/SRO-LECs with *R*o = 30 (B30) behaves similar to the B20 bilayer, as observed in **Figure 13(b)**. In the high conduction state, the dominant mechanism is hopping tunneling (pink line), where the average distance between traps is about 0.15 nm, indicating a higher density of traps compared to the B20 sample (0.25 nm). When the current drops to the low conduction state, the dominating mechanism changes to the P-F conduction (blue line). The dielectric constant (ε_r) was estimated at 5.98, indicating a lower content of silicon related to B20 sample (8.61), as expected. However, when the EL emission starts, the conduction begins to be dominated by TAT (orange line). The traps depth was estimated at about 2.15 eV, very similar to that obtained in B20 sample (2.06) and very close to the depth at which are the centers K^0 (~2.1 eV) [64].

In summary, the conduction mechanism in the region of low electric fields at HCS is hopping for SRN/SRO bilayers. It was observed that when the nitrogen content in the SRO layer increases, the average distance between defects also increases either due to the defects passivation or due to the reduction of the Si-nps size. In the region of high electric fields at low conduction, both TAT and P-F mechanisms take place simultaneously. The trap depth, obtained by the TAT fit, was ~2.1 eV from the minimum of the conduction band for both bilayers (B20 and B30), which relates to the location of the centers K^0 in SRN film.

7. Conclusions

The compositional, structural, optical, and electro-optical properties of SRO, SRN films as well as combination of SRN/SRO bilayers deposited by LPCVD were studied. The EL of the SRN-LECs showed a broad emission spectrum where the maximum peak blueshifts when the polarity changed from reverse to forward bias. The EL spectrum was nearly similar to that of PL when LECs were forwardly biased and the silicon excess was increased. Analyzing the current-voltage characteristics, it was found that TAT was the main carrier transport mechanism in SRN films in both biases, where typical EL was observed. In SRO films, it was demonstrated that the silicon content affects the luminescence centers density obtaining the EL emission at lower electric field as the silicon excess increased. SRO with *R*o = 30 films exhibited the presence of structural defects like NOV, NBOHC, and E'_δ (Si↑Si=Si) centers, which produced blue to red PL band after thermal annealing. SRO with *R*o = 20 films showed mainly red PL produced by the presence of well-defined Si-ncs. It was found that SRO-LECs with *R*o = 30 shows an intense blue EL, after a resistance switching behavior was reached. The RS was originated by the annihilation of preferential conductive paths created by Si-nps and silicon nanoclusters through structural changes that result in a long spectral blueshift (~222 nm) between the PL and EL. On the other hand, the RS was not observed in

SRO-LECs with *R*o = 20 due to the well-defined Si-nps with 2.7 nm size. These well-defined Si-nps produce a better charge injection through multiple conductive paths enhancing an intense red EL, which is related mainly to defects at the Si-nps/SiOx interface. The transport mechanism was affected by the composition and structure of the films, being TAT and PF the dominant transport mechanism in SRO with *R*o = 30 and 20, respectively. When the SRN was deposited onto the SRO to form the bilayer, compositional and electro-optical changes were observed. The SRN/SRO layers showed a broad PL emission respect to a simple SRO or SRN layer. In addition, multiple defects or centers were responsible of PL emission. The same luminescent centers in SRN/SRO were present in SRO and SRN monolayers. SRN/SRO-LECs showed an intense UV EL at high electric fields related to indium ions radiation. The conduction mechanism in SRN/SRO bilayers was found to be dominated by Pool-Frenkel and TAT mechanisms at LCS, and hopping at HCS.

Acknowledgements

This work has been partially supported by the project CONACyT-180992. The authors acknowledge technicians Pablo Alarcon, Armando Hernández, and Victor Aca from INAOE and Luis Gerardo Silva from CIMAV.

Author details

Santiago A. Cabañas-Tay[1], Liliana Palacios-Huerta[2], Mariano Aceves-Mijares[2], Antonio Coyopol[1], Sergio A. Pérez-García[1], Liliana Licea-Jiménez[1], Carlos Domínguez[3] and Alfredo Morales-Sánchez[1]*

*Address all correspondence to: alfredo.morales@cimav.edu.mx

1 Advanced Materials Research Center (CIMAV), Monterrey-PIIT Apodaca, Nuevo León, México

2 Electronics Department, National Institute of Astrophysics Optics and Electronics Tonantzintla, Puebla, México

3 Microelectronics Institute of Barcelona (IMB-CNM, CSIC) Bellaterra, Barcelona, Spain

References

[1] Tseng C.-K., Lee M.-C. M., Hung H.-W., Huang J.-R., Lee K.-Y., Shieh J.-M., and Lin G.-R. Silicon-nanocrystal resonant-cavity light emitting devices for color tailoring. Journal of Applied Physics. 2012;111(7): 074512. DOI: 10.1063/1.3702793

[2] Zhiping Z., Bing Y., and Jurgen M. On-chip light sources for silicon photonics. Light: Science & Applications. 2015;4: e358. DOI: 10.1038/lsa.2015.131

[3] Berencén Y., Illera S., Rebohle L., Ramírez J. M., Wutzler R., Cirera A., Hiller D., Rodríguez J. A., Skorupa W., and Garrido B. Luminescence mechanism for Er^{3+} ions in a silicon-rich nitride host under electrical pumping. Journal of Physics D: Applied Physics. 2016;49(8): 085106. DOI: 10.1088/0022-3727/49/8/085106

[4] Canham L. T. Silicon quantum wire array fabrication by electrochemical and chemical dissolution of wafers. Applied Physics Letters. 1990;57:1046–1048. DOI: 10.1063/1.103561

[5] Delerue C., Allan G., and Lannoo M. Theoretical aspects of the luminescence of porous silicon. Physical Review B. 1993;48(15):11024–11036. DOI: 10.1103/PhysRevB.48.11024

[6] Barreto J., Morales A., Perálvarez M., Garrido B., and Domínguez C. Stoichiometry of silicon-rich dielectrics for silicon nanocluster formation. Physica Status Solidi (C). 2011;8(3):1610–1642. DOI: 10.1002/pssc.201000363

[7] Shih C.-F., Hsiao C.-Y., and Su K.-W. Enhanced white photoluminescence in silicon-rich oxide/SiO_2 superlattices by low-energy ion-beam treatment. Optics Express. 2013;21(13): 15888–15895. DOI: 10.1364/OE.21.015888

[8] Mohammed S., Nimmo M. T., Malko A. V., and Hinkle C. L. Chemical bonding and defect states of LPCVD grown silicon-rich Si_3N_4 for quantum dot applications. Journal of Vacuum Science & Technology A. 2014;32(2): 021507. DOI: 10.1116/1.4861338

[9] Liao W., Zeng X., Wen X. and Wen Y. Tunable photoluminescence of Si-rich nitride films with silicon quantum dots by changing the total pressure. International Photonics and Optoelectronics. 2015; JW3A.33. DOI: 10.1364/OEDI.2015.JW3A.33

[10] Vlasukova L. A., Komarov F. F., Parkhomenko I. N., Milchanin O. V., Makhavikou M. A., Mudryi A. V., Żuk, J., Kopychiński P., and Togambayeva A. K. Visible photoluminescence of non-stoichiometric silicon nitride films: The effect of annealing temperature and atmosphere. Journal of Applied Spectroscopy. 2015;82(3): 386–389. DOI: 10.1007/s10812-015-0117-9

[11] Lin G.-R., Lin C.-J., and Lin C.-K. Enhanced Fowler-Nordheim tunneling effect in nanocrystallite Si based LED with interfacial Si nano-pyramids. Optics Express. 2007;15(5):2555–2563. DOI: 10.1364/OE.15.002555

[12] Lin Y.-H., Wu C.-L., Pai Y.-H., and Lin G.-R. A 533-nm self-luminescent Si-rich SiNx/SiOx distributed Bragg reflector. Optics Express. 2011;19(7):6563–6570. DOI: 10.1364/OE.19.006563

[13] Nishi H., Tsuchizawa T., Shinojima H., Watanabe T., Itabashi S-I., Kou R., Fukuda H., and Yamada K. Low-polarization-dependent silica waveguide monolithically integrated on SOI photonic platform. Journal of Lightwave Technology. 2013;31(11):1821–1827. DOI: 10.1109/JLT.2013.2256880

[14] Cheng C.-H., Lien Y.-C., and Wu C.-L., and Lin G.-R. Mutlicolor electroluminescent Si quantum dots embedded in SiOx thin film MOSLED with 2.4% external quantum efficiency. Optics Express. 2013;21(1): 391–403. DOI: 10.1364/OE.21.000391

[15] Zimmermann H., editors. Integrated Silicon Optoelectronics. 2nd ed. Germany: Springer-Verlag Berlin Heidelberg; 2010. 406 p. DOI: 10.1007/978-3-642-01521-2

[16] Pavesi L., Gaponenko S., and Dal Negro L., editors. Towards the First Silicon Laser. 1st ed. Dordrecht: Kluwer Academic Publishers; 2003. 490 p. DOI: 10.1007/978-94-010-0149-6

[17] Klak M. M., Zatryb G., Wojcik J., Misiewicz J., Mascher P., and Podhorodecki A. Mechanism of enhanced photoluminescence of Tb ions in hydrogenated silicon-rich silicon oxide films. Thin Solid Films. 2016;611: 62–67. DOI: 10.1016/j.tsf.2016.04.050

[18] Barbagiovanni E. G., Lockwood D. J., Simpson P. J., and Goncharova, L. V. Quantum confinement in Si and Ge nanostructures. Journal of Applied Physics. 2012;111(3): 034307. DOI: 10.1063/1.3680884

[19] Iacona F., Franzò G., and Spinella C. Correlation between luminescence and structural properties of Si nanocrystals. Journal of Applied Physics. 2000;87(3): 1295–1303. DOI: 10.1063/1.372013

[20] Kim T.-W., Cho C.-H., Kim B.-H., and Park S.-J. Quantum confinement effect in crystalline silicon quantum dots in silicon nitride grown using SiH_4 and NH_3. Applied Physics Letters. 2006;88(12): 123102. DOI: 10.1063/1.2187434

[21] Qin G. G., Li A. P., Zhang B. R., and Li B.-C. Visible electroluminescence from semitransparent Au film/extra thin Si-rich silicon oxide film/p-Si structure. Journal of Applied Physics. 1995;78(3): 2006–2009. DOI: 10.1063/1.360175

[22] Lin G.-R., and Lin C.-J. Improved blue-green electroluminescence of metal-oxide-semiconductor diode fabricated on multirecipe Si-implanted and annealed SiO_2/Si substrate. Journal of Applied Physics. 2004;95(12): 8484–8486. DOI: 10.1063/1.1739283

[23] Liu Y., Chen T. P., Ding L., Yang M., Wong J. I., Ng C. Y., Yu S. F., Li Z. X., Yuen C., Zhu F. R., Tan M. C., and Fung S. Influence of charge trapping on electroluminescence from Si-nanocrystal light emitting structure. Journal of Applied Physics. 2007;101(10): 104306. DOI: 10.1063/1.2713946

[24] Liao L.-S., Bao X.-M., Li N.-S., Zheng X.-Q., and Min N.-B. Visible electroluminescence from Si^+-implanted SiO_2 films thermally grown on crystalline Si. Solid State Communications. 1996;97(12): 1039–1042. DOI: 10.1016/0038-1098(95)00846-2

[25] Wang T., Wei D. Y., Sun H. C., Liu Y., Chen D. Y., Chen G. R., Xu J., Li W., Ma Z. Y., Xu L., and Chen K. J. Electrically driven luminescence of nanocrystalline Si/SiO_2 multilayers on various substrates. Physica E: Low-dimensional Systems and Nanostructures. 2009;41(6): 923–926. DOI: 10.1016/j.physe.2008.08.001

[26] López-Vidrier J., Berencén Y., Hernández S., Blázquez O., Gutsch S., Laube J., Hiller D., Löper P., Schnabel M., Janz S., Zacharias M., and Garrido B. Charge transport and electroluminescence of silicon nanocrystals/SiO_2 superlattices. Journal of Applied Physics. 2013;114(16): 163701. DOI: 10.1063/1.4826898

[27] Cho K. S., Park N.-M., Kim T.-Y., Kim K.-H., Shin J.-H., Sung G. Y., and Shin J. H. High efficiency visible electroluminescence from silicon nanocrystals embedded in silicon nitride using a transparent doping layer. Applied Physics Letters. 2006;88(20): 209904. DOI: 10.1063/1.2205754

[28] Huang R., Chen K., Qian B., Chen S., Li W., Xu J., Ma Z., and Huang X. Oxygen induced strong green light emission from low-temperature grown amorphous silicon nitride films. Applied Physics Letters. 2006;89(22): 221120. DOI: 10.1063/1.2399393

[29] Huang R., Chen K., Dong H., Wang D., Ding H., Li W., Xu J., Ma Z., and Xu L. Enhanced electroluminescence efficiency of oxidized amorphous silicon nitride light-emitting devices by modulating Si/N ratio. Applied Physics Letters. 2007;91(11): 111104. DOI: 10.1063/1.2783271

[30] Cen Z. H., Chen T. P., Liu Z., Liu Y., Ding L., Yang M., Wong J. I., Yu S. F., and Goh W. P. Electrically tunable white-color electroluminescence from Si-implanted silicon nitride thin film. Optics Express. 2010;18(19): 20439–20444. DOI: 10.1364/OE.18.020439

[31] Warga J., Li R., Basu S. N., and Dal Negro L. Electroluminescence from silicon-rich nitride/silicon superlattice structures. Applied Physics Letters. 2008;93(15): 151116. DOI: 10.1063/1.3003867

[32] Tai H. Y., Lin Y. H., and Lin G. R. Wavelength-shifted yellow electroluminescence of Si quantum-dot embedded 20-pair SiNx/SiOx superlattice by Ostwald ripening effect. IEEE Photonics Journal. 2013;5(1): 6600110. DOI: 10.1109/JPHOT.2012.2232285

[33] González-Fernández A. A., Juvert J., Aceves-Mijares M., and Domínguez C. Monolithic integration of a silicon-based photonic transceiver in a CMOS Process. IEEE Photonics Journal. 2016;8(1):1–13. DOI: 10.1109/JPHOT.2015.2505144

[34] Cabañas-Tay S. A., Palacios-Huerta L., Luna-López J. A., Aceves-Mijares M., Alcántara-Iniesta S., Pérez-García S. A., and Morales-Sánchez A. Analysis of the luminescent centers in silicon rich silicon nitride light-emitting capacitors. Semiconductor Science and Technology. 2015;30(6):065009. DOI: 10.1088/0268-1242/30/6/065009

[35] Tsu D. V., Lucovsky G., Mantini M. J., and Chao S. S. Deposition of silicon oxynitride thin films by remote plasma enhanced chemical vapor deposition. Journal of Vacuum Science & Technology A. 1987;5(4):1998–2002. DOI: 10.1116/1.574902

[36] Vuillod J. Preparation and characterization of plasma enhanced chemical vapor deposited silicon nitride and oxynitride films. Journal of Vacuum Science & Technology A. 1987;5(4):1675–1679. DOI: 10.1116/1.574545

[37] Debieu O., Nalini R. P., Cardin J., Portier X., Perrière J., and Gourbilleau F. Structural and optical characterization of pure Si-rich nitride thin films. Nanoscale Research Letters. 2013;8(1): 1–13. DOI: 10.1186/1556-276X-8-31

[38] Lin K-C, and Lee S-C. The structural and optical properties of a-SiNx:H prepared by plasma-enhanced chemical-vapor deposition. Journal of Applied Physics. 1992;72(11):5474–5482. DOI: 10.1063/1.351992

[39] Scardera G., Puzzer T., Conibeer G., and Green M. A. Fourier transform infrared spectroscopy of annealed silicon-rich silicon nitride thin films. Journal of Applied Physics. 2008;104(10):104310. DOI: 10.1063/1.3021158

[40] Tsu D. V., Lucovsky G., and Mantini M. J. Local atomic structure in thin films of silicon nitride and silicon diimide produced by remote plasma-enhanced chemical-vapor deposition. Physical Review B. 1986;33(10):7069–7076. DOI: 10.1103/PhysRevB.33.7069

[41] Aceves-Mijares M., Espinosa-Torres N. D., Flores-Gracia F., González-Fernández A. A., López-Estopier R., Román-López S., Pedraza G., Domínguez C., Morales A., and Falcony C. Composition and emission characterization and computational simulation of silicon rich oxide films obtained by LPCVD. Surface and Interface Analysis. 2014;46: 216–223. DOI:10.1002/sia.5212

[42] Fazio E., Barletta E., Barreca F., Neri F., and Trusso S. Investigation of a nanocrystalline silicon phase embedded in SiOx thin films grown by pulsed laser deposition. Journal of Vacuum Science & Technology B. 2005;23(2):519–524. DOI: 10.1116/1.1880252

[43] Schliwinski H. –J., Schnakenberg U., Windbracke W., Neff H., and Lange P. Thermal annealing effects on the mechanical properties of plasma-enhanced chemical vapor deposited silicon oxide films. Journal of the Electrochemical Society. 1992;139(6):1730–1735. DOI: 10.1149/1.2069484

[44] Pai P. G., Chao S. S., Takagi Y., and Lucovsky G. Infrared spectroscopic study of SiOx films produced by plasma enhanced chemical vapor deposition. Journal of Vacuum Science & Technology A. 1986;4(3):689–694. DOI: 10.1116/1.573833

[45] Diniz J. A., Tatsch P. J., and Pudenzi M. A. A. Oxynitride films formed by low energy NO^+ implantation into silicon. Applied Physics Letters. 1996;69(15):2214–2215. DOI: 10.1063/1.117169

[46] Palacios-Huerta L., Cabañas-Tay S. A., Luna-López J. A., Aceves-Mijares M., Coyopol A., and Morales-Sánchez A. Effect of the structure on luminescent characteristics of SRO-based light emitting capacitors. Nanotechnology. 2015;26(39):395202. DOI: 10.1088/0957-4484/26/39/395202

[47] Morales-Sánchez A., Monfil-Leyva K., González A. A., Aceves-Mijares M., Carrillo J., Luna-López J. A., Domínguez C., Barreto J., and Flores-Gracia F. J. Strong blue and red luminescence in silicon nanoparticles based light emitting capacitors. Applied Physics Letters. 2011;99(17):171102. DOI: 10.1063/1.3655997

[48] Lin G.-R., Lin C.-J., and Kuo H.-C. Improving carrier transport and light emission in a silicon-nanocrystal based MOS light-emitting diode on silicon nanopillar array. Applied Physics Letters. 2007;91(9):093122. DOI: 10.1063/1.2778352

[49] Dohnalová K., Ondič L., Kusová K., Pelant I., Rehspringer J. L., and Mafouana R.-R. White-emitting oxidized silicon nanocrystals: Discontinuity in spectral development with reducing size. Journal of Applied Physics. 2010;107(5):053102. DOI: 10.1063/1.3289719

[50] Wang X., Zhang R. Q., Lee S. T., Niehaus T. A., and Frauenheim T. Unusual size dependence of the optical emission gap in small hydrogenated silicon nanoparticles. Applied Physics Letters. 2007;90(12):123116. DOI: 10.1063/1.2715101

[51] Cueff S., Labbé C., Jambois O., Berencén Y., Kenyon A. J., Garrido B., and Rizk R. Structural factors impacting carrier transport and electroluminescence from Si nanocluster-sensitized Er ions. Optics Express. 2012;20(20): 22490–22502. DOI: 10.1364/OE.20.022490

[52] Kiebach R., Yu Z., Aceves-Mijares M., Bian D., and Du J. The deposition and control of self-assembled silicon nano islands on crystalline silicon. International Journal of High Speed Electronics and Systems. 2008;18(4):901–910. DOI: 10.1142/S0129156408005862

[53] Park N.-M., Choi C.-J., Seong T.-Y., and Park S.-J. Quantum confinement in amorphous silicon quantum dots embedded in silicon nitride. Physical Review Letters. 2001;86(7):1355–1357. DOI: 10.1103/PhysRevLett.86.1355

[54] Wang Y. Q., Wang Y. G., Cao L., and Cao Z. X. High-efficiency visible photoluminescence from amorphous silicon nanoparticles embedded in silicon nitride. Applied Physics Letters. 2003;83(17):3474–3476. DOI: 10.1063/1.1621462

[55] Park N.-M., Kim T.-S., and Park S.-J. Band gap engineering of amorphous silicon quantum dots for light-emitting diodes. Applied Physics Letters. 2001;78(17):2575–2577. DOI: 10.1063/1.1367277

[56] Mercaldo L. V., Veneri P. D., Esposito E., Massera E., Usatii I., and Privato C. PECVD in-situ growth of silicon quantum dots in silicon nitride from silane and nitrogen. Materials Science and Engineering B. 2009;159–160:77–79. DOI: 10.1016/j.mseb.2008.09.029

[57] Liao W., and Zeng X., Wen X., Chen X., and Wang W. Annealing and excitation dependent photoluminescence of silicon rich silicon nitride films with silicon quantum dots. Vacuum. 2015;121: 147–151. DOI: 10.1016/j.vacuum.2015.08.002

[58] Xie M., Li D., Wang F., and Yang D. Luminescence properties of silicon-rich silicon nitride films and light emitting devices. ECS Transactions. 2011;35(18):3–19. DOI: 10.1149/1.3647900

[59] Dal Negro L., Li R., Warga J., and Basu S. N. Sensitized erbium emission from silicon-rich nitride/silicon superlattice structures. Applied Physics Letters. 2008;92(18):181105. DOI: 10.1063/1.2920435

[60] Sahu B. S., Delachat F., Slaoui A., Carrada M., Ferblantier G., Muller D. Effect of annealing treatments on photoluminescence and charge storage mechanism in silicon-rich SiNx:H films. Nanoscale Research Letters. 2011;6(1):1–10. DOI: 10.1186/1556-276X-6-178

[61] Giorgis F., Vinegoni C., and Pavesi L. Optical absorption and photoluminescence properties of a-Si_{1-x}:H films deposited by plasma-enhanced cvd. Physical Review B. 2000;61(7):4693–4698. DOI: 10.1103/PhysRevB.61.4693

[62] Warren W. L., Robertson J., and Kanicki J. Si and N dangling bond creation in silicon nitride thin films. Applied Physics Letters. 1993;63(19):2685–2687. DOI: 10.1063/1.110420

[63] Warren W. L., Lenahan P. M., and Curry S. E. First observation of paramagnetic nitrogen dangling-bond centers in silicon nitride. Physical Review Letters. 1990;65(2):207–210. DOI: 10.1103/PhysRevLett.65.207

[64] Robertson J., and Powell M. J. Gap states in silicon nitride. Applied Physics Letters. 1984;44(4):415–417. DOI: 10.1063/1.94794

[65] Liu Y., Zhou Y., Shi W., Zhao L., Sun B., and Ye T. Study of photoluminescence spectra of Si-rich SiNx films. Materials Letters. 2004;58(19):2397–2400. DOI: 10.1016/j.matlet.2004.02.015

[66] Nguyen P. D., Kepaptsoglou D. M., Ramasse Q. M., Sunding M. F., Vestland L. O., Finstad T. G., and Olsen A. Impact of oxygen bonding on the atomic structure and photoluminescence properties of Si-rich silicon nitride thin films. Journal of Applied Physics. 2012;112(7):073514. DOI: 10.1063/1.4756998

[67] Hao X. J., Podhorodecki A. P., Shen Y. S., Zatryb G., Misiewicz J., and Green M. A. Effects of Si-rich oxide layer stoichiometry on the structural and optical properties of Si QD/SiO_2 multilayer films. Nanotechnology. 2009;20(48):485703. DOI: 10.1088/0957-4484/20/48/485703

[68] Lai B. H., Cheng C. H., and Lin G. R.. Multicolor ITO/SiOx/p-Si/Al Light Emitting Diodes With Improved Emission Efficiency by Small Si Quantum Dots. IEEE Journal of Quantum Electronics. 2011;47(5):698–704. DOI: 10.1109/JQE.2011.2109699

[69] González-Fernández A. A., Aceves-Mijares M., Morales-Sánchez A., and Monfil-Leyva K. Intense whole area electroluminescence from low pressure chemical vapor deposition-silicon-rich oxide based light emitting capacitors. Journal of Applied Physics. 2010;108(4):043105. DOI: 10.1063/1.3465335

[70] Salh R. Defect Related Luminescence in Silicon Dioxide Network: A Review. In: Prof. Sukumar Basu, editor. Crystalline Silicon—Properties and Uses. Umeå, Sweden: InTech; 2011. DOI: 10.5772/22607

[71] Rodríguez J. A., Vásquez-Agustín M. A., Morales-Sánchez A., and Aceves-Mijares M. Emission mechanisms of Si nanocrystals and defects in SiO_2 materials. Journal of Nanomaterials. 2014;2014:409482. DOI: 10.1155/2014/409482

[72] González-Fernández A. A., Juvert J., Aceves-Mijares M., Llobera A., and Domínguez C. Influence of silicon binding energy on photoluminescence of Si-implanted silicon dioxide. ECS Transactions. 2012;49(1):307–314. DOI: 10.1149/04901.0307ecst

[73] Perálvarez M., Carreras J., Barreto J., Morales A., Domínguez C., and Garrido B. Efficiency and reliability enhancement of silicon nanocrystal field-effect luminescence from nitride-oxide gate stacks. Applied Physics Letters. 2008;92(24):241104. DOI: 10.1063/1.2939562

[74] Parker C. G., Lucovsky G., and Hauser J. R. Ultrathin oxide-nitride gate dielectric MOSFET's. IEEE Electron Device Letters. 1998;19(4):106–108. DOI: 10.1109/55.663529

[75] Wang X., Huang R., Song C., Guo Y., and Song J. Effect of barrier layers on electroluminescence from Si/SiOxNy multilayer structures. Applied Physics Letters. 2013;102(8):081114. DOI: 10.1063/1.4794079

[76] Berencén Y., Ramírez J. M., Jambois O., Domínguez C., Rodríguez J. A., and Garrido B. Correlation between charge transport and electroluminescence properties of Si-rich oxide/nitride/oxide-based light emitting capacitors. Journal of Applied Physics. 2012;112(10):109901. DOI: 10.1063/1.4768249

[77] Pei Z., Chang Y. R., and Hwang H. L. White electroluminescence from hydrogenated amorphous-SiNx thin films. Applied Physics Letters. 2002;80(16):2839–2841. DOI: 10.1063/1.1473230

[78] Li D., Huang J., and Yang D. Enhanced electroluminescence of silicon-rich silicon nitride light-emitting devices by NH_3 plasma and annealing treatment. Physica E: Low-dimensional Systems and Nanostructures. 2009;41(6):920–922. DOI: 10.1016/j.physe.2008.08.024

[79] Morales-Sánchez A., Barreto J., Domínguez C., Aceves-Mijares M., and Luna-López J. A. The mechanism of electrical annihilation of conductive paths and charge trapping in silicon-rich oxides. Nanotechnology. 2009;20(4):045201. DOI: 10.1088/0957-4484/20/4/045201

[80] Morales-Sánchez A., Barreto J., Domínguez C., Aceves-Mijares M., Perálvarez M., Garrido B., and Luna-López J. A. DC and AC electroluminescence in silicon nanoparticles embedded in silicon-rich oxide films. Nanotechnology. 2010;21(8):085710. DOI: 10.1088/0957-4484/21/8/085710

[81] Yao J., Sun Z., Zhong L., Natelson D., and Tour J. M. Resistive switches and memories from silicon oxide. Nano Letters. 2010;10(10):4105–4110. DOI: 10.1021/nl102255r

[82] Yao J., Zhong L., Natelson D., and Tour J. M. In situ imaging of the conducting filament in a silicon oxide resistive switch. Scientific Reports. 2012;2:242. DOI: 10.1038/srep00242

[83] Mehonic A., Vrajitoarea A., Cueff S., Hudziak S., Howe H., Labbé C., Rizk R., Pepper M., and Kenyon A. J. Quantum conductance in silicon oxide resistive memory devices. Scientific Reports. 2013;3:2708. DOI: 10.1038/srep02708

[84] Mehonic A., Cueff S., Wojdak M., Hudziak S., Labbé C., Rizk R., and Kenyon A. J. Electrically tailored resistance switching in silicon oxide. Nanotechnology. 2012;23(45):455201. DOI: 10.1088/0957-4484/23/45/455201

[85] González-Fernández A. A., Juvert J., Aceves-Mijares M., Llobera A., and Domínguez C. Influence by layer structure on the output EL of CMOS compatible silicon-based light emitters. IEEE Transactions on Electron Devices. 20123;60(6): 1971–1974. DOI: 10.1109/TED.2013.2258158

[86] Wang D.-C., Chen J.-R., Zhu J., Lu C.-T., and Lu M. On the spectral difference between electroluminescence and photoluminescence of Si nanocrystals: a mechanism study of

electroluminescence. Journal of Nanoparticle Research. 2013;15(11):1–7. DOI: 10.1007/s11051-013-2063-x

[87] Yin X., Wang S., Li L., Mu G., Tang Y., Duan W., and Yi L. Intense deep-blue electroluminescence from ITO/Y_2O_3/Ag structure. Optics Express. 2015;23(14):18092–18097. DOI: 10.1364/OE.23.018092

[88] Huang R., Song J., Wang X., Guo Y. Q., Song C., Zheng Z. H., Wu X. L., and Chu P. Origin of strong white electroluminescence from dense Si nanodots embedded in silicon nitride. Optics Letters. 2012;37(4):692–694. DOI: 10.1364/OL.37.000692

[89] Tao Y., Zheng J., Zuo Y., Xue C., Cheng B., and Wang Q. Enhanced current transportation in silicon-riched nitride (SRN)/silicon-riched oxide (SRO) multilayer nanostructure. Nano-Micro Letters. 2012;4(4): 202–207. DOI: 10.1007/BF03353715

[90] Huang R., Wang D. Q., Ding H. L., Wang X., Chen K. J., Xu J., Guo Y. Q., Song J., and Ma Z. Y. Enhanced electroluminescence from SiN-based multilayer structure by laser crystallization of ultrathin amorphous Si-rich SiN layers. Optics Express. 2010;18(2):1144–1150. DOI: 10.1364/OE.18.001144

[91] Vila M., Prieto C., and RamÍrez R. Electrical behavior of silicon nitride sputtered thin films. Thin Solid Films. 2004;459(1–2):195–199. DOI: 10.1016/j.tsf.2003.12.082

[92] Ramírez J. M., Berencén Y., López-Conesa L., Rebled J. M., Peiró F., and Garrido B. Carrier transport and electroluminescence efficiency of erbium-doped silicon nanocrystal superlattices. Applied Physics Letters. 2013;103(8):081102. DOI: 10.1063/1.4818758

[93] Perera R., Ikeda A., Hattori R., and Kuroki Y. Trap assisted leakage current conduction in thin silicon oxynitride films grown by rapid thermal oxidation combined microwave excited plasma nitridation. Microelectronic Engineering. 2003;65(4):357–370. DOI: 10.1016/S0167-9317(02)01025-0

[94] Anopchenko A., Marconi A., Moser E., Prezioso S., Wang M., Pavesi L., Pucker G., and Bellutti P. Low-voltage onset of electroluminescence in nanocrystalline-Si/SiO2 multilayers. Journal of Applied Physics. 2009;106(3):033104. DOI: 10.1063/1.3194315

IntechOpen